Optimized design of frequency dividers based on varactor−inductor cells

Mabel Pontón, *Member, IEEE*, Almudena Suárez, *Fellow, IEEE*

Abstract— **This paper presents an in−depth analysis of a recently proposed frequency divider by two, which is based on a parallel connection of varactor−inductor cells, in a differential operation at the subharmonic frequency. The analytical study of a single−cell divider enables the derivation of a real equation governing the circuit at the frequency−division threshold. This equation is used for a detailed investigation of the impact of the circuit elements on the input−amplitude threshold and the frequency bandwidth. Insight provided by the analytical formulation enables the derivation of a thorough synthesis methodology for multiple−cell dividers, usable in harmonic balance with an auxiliary generator at the divided frequency. Two different applications of this topology are demonstrated: a dual−phase divider and a dual−band frequency divider. The former is obtained by using Marchand balun to deliver 180º phase−shifted signals to the two dividers. On the other hand, the dual−band divider is based on a novel configuration which combines cells with parallel varactors and cells with series varactors. Departing from the optimization procedure of the single−band divider, a simple synthesis method is presented to center the two division bands at the desired values. The techniques have been applied to three prototypes at 2.15 GHz, 1.85 GHz and 1.75 GHz / 3.95 GHz, respectively.**

Index Terms— **Frequency dividers, dual−phase generation, dual−band frequency division, phase noise.**

I. INTRODUCTION

THE works [1]-[2] propose a frequency divider topology based on the use of two parallel nonlinear transmission lines (NLTL) connected through back to back diodes [Fig. 1(a)]. The two NLTLs behave like a reflective distributed resonator, since the odd−mode subharmonic oscillation terminates in a virtual ground at both ends, so the output signal is extracted from internal cells by means of a buffer [1]-[2]. The subharmonic component is sustained by the gain exhibited by the varactors under the pump signal at $\omega_{in}=2\omega$ and, in this manner, a standing wave [1]-[2] is formed through the distributed resonator. This divider configuration exhibits zero static−power consumption [2]-[3], which is an interesting quality since, in practical applications, the frequency divider usually consumes a significant portion of the frequency synthesizer power [1]-

[3]. Another advantage comes from the absence of a free−running oscillation, which in injection−locked dividers [4]-[6], gives rise to undesired mixer like regimes [6]-[7] outside the division band. In addition, the absence of an oscillation enables lower phase−noise spectral density at large offset frequency from the carrier [1]-[2], [8].

The works [1]-[2] have demonstrated that a synchronous propagation of the pump and subharmonic signals is beneficial for the energy transfer from the pump to the subharmonic signal. This requires a minimization of the dispersion effect, which is achieved through the use of an additional capacitor c_c connected between the middle node of the back−to−back diodes and ground (Fig. 1). The capacitor decreases the average capacitance at 2ω, but does not directly affect the odd harmonics of the subharmonic signal, due to the circuit symmetry. The analysis in [1]-[2] departs from a continuous transmission−line model [9], which is followed by several corrections accounting for dispersion and mismatch at the pump frequency, among other effects.

An alternative investigation is presented in this work. It is based on a detailed circuit−level analysis of the new divider topology, carried out in two different ways: analytically [10], in the case of a single−cell divider, and through harmonic balance (HB), complemented with an auxiliary−generator technique [6]-[7], in the case of multiple cells. Using the analytical formulation, a single equation, governing the global behavior of frequency divider at the division threshold, is derived, which will enable an understanding of the impact of each divider element on the input−sensitivity curve. With this insight, an optimization procedure, intended for HB simulators and applicable to dividers with multiple cells, will be developed.

Novel applications of the divider based on varactor−inductor cells will be investigated. One of them is a dual−phase divider, based on the use of two of these dividers, together with a Marchand balun [11] for a simple generation of in−phase and quadrature signals. Possible applications include quadrature modulation and quadrature down conversion [12]. The Marchand balun provides two signals with 180º phase shift, which are introduced in the differential frequency dividers. Then the frequency division inherently gives rise to a 90º phase shift [12] between equivalent nodes of the two divider circuits.

A dual−band frequency divider, based on the use of two different types of differential inductor−varactor cells, is also investigated. One section is composed of cells having the varactors in a parallel connection, whereas the other section

is composed of cells having the varactors in a series connection. Unlike previously presented dual−band frequency dividers [13], there is no oscillation in the absence of an input signal. This avoids undesired self−oscillating mixer regimes below the division threshold and between the division bands. The dual band design will allow coping with the major limitation of this novel kind of frequency dividers, which is the frequency bandwidth. As will be shown, the two coexistent division bands can be tuned, and even preset, with a simulation procedure that relies on the properties revealed by the analytical formulation. In this way, the designer can take advantage of the two interesting characteristics of this novel kind of dividers, which are the zero static power consumption and the low phase−noise spectral density [1]-[2].

The paper is organized as follows. Section II presents the analytical study of a single−cell divider, with a detailed investigation of the impact of each element of the circuit topology. Section III describes a dual−phase divider, based on the use of a Marchand balun. Section IV presents the synthesis of a dual−band frequency divider.
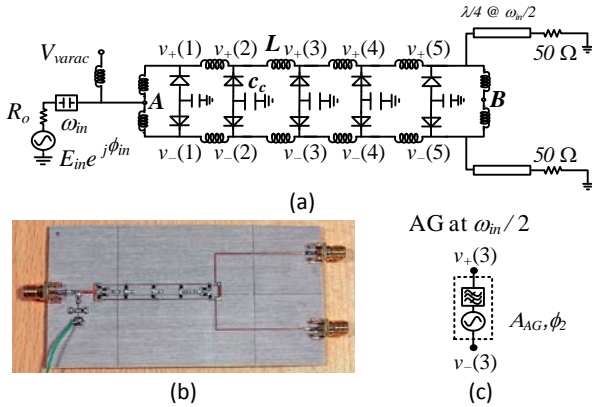

(a)

(b)   (c)

Fig. 1 Multi−cell frequency divider. (a) Schematic of a multi−cell divider, enabling an odd−mode subharmonic oscillation. The number n in the notation $v_+(n) - v_-(n)$ refers to the order of the back−to−back diode pairs. There is a total of $N = 5$ pairs. (b) Photograph of the prototype built in Rogers 4003C substrate $(\varepsilon_r = 3.38, H = 0.508 \text{ mm})$. In the different prototypes, individual signals are extracted with impedance transformers (as in the photograph) or with a source−follower buffer based on the transistor NE3210S01. (c) Auxiliary generator (AG) used to simulate and optimize the divider in HB. It is connected between the nodes $v_+(3)$ and $v_-(3)$ in the schematic of (a).

II. ANALYSIS OF THE DIVISION THRESHOLD

The dependence of the input−amplitude division threshold on the various circuit elements and parameters will be studied in the two cases of a single−cell divider and a multi−cell divider.

A. Single−cell divider

For the analytical formulation of a single−cell divider, the varactor diode will be modeled by a nonlinear capacitor in series with a loss resistor R_D [Fig. 2(a)]. Limiting the analysis to the subharmonic and input frequencies, $\omega_{in}/2$ and ω_{in}, the voltage waveform across the nonlinear capacitor will be approximated with the following truncated Fourier series:

$$v(t) = Ve^{j\omega t} + Ve^{-j\omega t} + V_2 e^{j(2\omega t + \phi_2)} + V_2 e^{-j(2\omega t + \phi_2)} \quad (1)$$

where $\omega = \omega_{in}/2$ is the subharmonic frequency and the phase origin is taken at ω. Assuming a moderate input amplitude, it will be possible to model the varactor capacitance with a first-order Taylor series $c(v) = c_o + bv$ [1]-[2]. Replacing the waveform (1) into $c(v) = c_o + bv$, one obtains the current entering the nonlinear capacitor, in time domain. The two−sided Fourier−series expression of this current has the component I_1 at ω and the component I_2 at 2ω, which are given by:

$$
\begin{aligned}
I_1 &= \left[j\omega(c_o + bV_2 \cos\phi_2) - \omega b V_2 \sin\phi_2 \right] V \\
I_2 &= j\omega\left(2c_o V_2 e^{j\phi_2} + bV^2\right)
\end{aligned} \quad (2)
$$

The ratio between the current I_1 and voltage V provides the input admittance function, Y_N, exhibited by the nonlinear capacitor at the subharmonic frequency ω:

$$Y_N = \frac{I_1}{V} = j\omega(c_o + bV_2 \cos\phi_2) - \omega b V_2 \sin\phi_2 \quad (3)$$

As gathered from (3), under a pump signal at ω_{in}, the nonlinear capacitance will exhibit negative conductance at $\omega_{in}/2$ provided that the condition $-\omega b V_2 \sin\phi_2 < 0$ is fulfilled. To formulate the divider equations, one should take into account the symmetry properties of the circuit topology. Assuming an odd mode subharmonic oscillation (180º phase shift between the two branches), the middle points A and B are virtual short circuits at the subharmonic frequency [Fig. 2(a)], which leads to the schematic of Fig. 2(b) at the subharmonic frequency. Applying Kirchoff's laws to this equivalent circuit, one obtains:

$$V + \left(R_D + j\frac{L\omega}{2}\right)I_1 = V + Z_a I_1 = 0 \quad (4)$$

where $Z_a = R_D + jL\omega/2$. On the other hand, as gathered from Fig. 2(a), the point B is a virtual open circuit at the input frequency $\omega_{in} = 2\omega$. Taking also into account the input equivalent network at 2ω, shown in Fig. 2(c), one obtains the following equation at the input frequency:

$$
\begin{aligned}
V_2 e^{j\phi_2} &+ Z_p(\omega)I_2 - E_{in}e^{j\phi_{in}} = \\
&= V_2 e^{j\phi_2} + Z_p(\omega)j\omega\left(2c_o V_2 e^{j\phi_2} + bV^2\right) - E_{in}e^{j\phi_{in}} = 0
\end{aligned} \quad (5)
$$

where E_{in} and ϕ_{in} are the amplitude and phase of the input source (considering a two−sided spectrum), $Z_p = R_p + j[L\omega_{in} - 2/(c_c\omega_{in})]$, $R_p = 2R_o + R_D$ and $R_o = 50 \, \Omega$. Note that R_o and the capacitor c_c only affect the equation (5), at $\omega_{in} = 2\omega$. Dividing both terms of (4) by V and using the definition of Y_N in (3), one obtains:

$$Y_T = \frac{1}{R_D + jL\omega/2} + Y_N =$$

$$= \frac{1}{R_D + jL\omega/2} + j\omega\left(c_o + bV_2\cos\phi_2\right) - \omega bV_2\sin\phi_2 = 0 \qquad (6)$$

The function Y_T agrees with the total−admittance function at the subharmonic component ω, calculated at node 2 of the equivalent circuit in Fig. 2(b). It is the addition of Y_N and the admittance of the series branch composed by R_D and $L/2$. Fulfillment of condition (6), $Y_T = 0$, implies the existence of a self−sustained subharmonic oscillation, due to the energy flow from the input pump at ω_{in} to the subharmonic signal [1]. The frequency division by 2 is enabled by the negative conductance at $\omega_{in}/2$ and the resonance effects inherent to the complex equation (6).

Dividing the two terms in (6) by $Y_N/(R_D + jL\omega/2)$ one obtains the following relationship:

$$j\frac{L\omega}{2} + R_D + \frac{1}{Y_N} = 0 \qquad (7)$$

Now, dividing all the terms of (7) by $(Y_N^{-1} + R_D)jL\omega/2$, one obtains an alternative expression for the subharmonic−oscillation condition:

$$\frac{2}{jL\omega} + \frac{1}{R_D + \frac{1}{Y_N}} = \frac{2}{jL\omega} + Y_1 = 0 \qquad (8)$$

where Y_1 is the total admittance function between the diode terminals, given by:

$$Y_1 = \frac{1}{R_D + \frac{1}{Y_N}} = \frac{1}{R_D + \left(j\omega c_o + j\omega b\overline{V}_2\right)^{-1}} \qquad (9)$$

and $\overline{V}_2 = V_2 e^{j\phi_2}$ is the voltage component at the input frequency. The bar stresses the fact that this voltage has a phase value ϕ_2, unlike the subharmonic voltage V, where the phase−reference is established. Note that the total varactor−admittance function Y_1 includes the effect of the loss resistance R_D. Equation (8) agrees with the total−admittance function at the subharmonic component ω, calculated at node 1 of the equivalent circuit in Fig. 2(b). The use of a frequency−division condition in terms of the varactor admittance (including R_D) will facilitate the extension of this condition to multiple cells, presented later in this section.

The limit condition for frequency−divider operation (division threshold) corresponds to a subharmonic amplitude tending to zero $V \to 0$. This agrees with the condition for a *flip bifurcation* [6]−[7], [14]. Splitting (6) [or, equivalently, (8)] into real and imaginary parts, one can calculate the voltage $\overline{V}_2 = V_2 e^{j\phi_2}$ at ω_{in} in the presence of a frequency division, which will be denoted as $\overline{V}_{2o} = V_{2o}e^{j\phi_{2o}}$. This is given by:

$$V_{2o}\cos\phi_{2o} = \frac{L/2}{b\left[R_D^2 + (L\omega_{in}/4)^2\right]} - \frac{c_o}{b} \qquad (a)$$

$$V_{2o}\sin\phi_{2o} = \frac{2R_D}{\omega_{in}b\left[R_D^2 + (L\omega_{in}/4)^2\right]} \qquad (b)$$

$$(10)$$

From inspection of (10), the voltage $\overline{V}_{2o} = V_{2o}e^{j\phi_{2o}}$ does not depend on E_{in}. For a fixed varactor model, it depends on the inductor L and the input frequency ω_{in}, so it can be expressed as $V_{2o}(L,\omega_{in})$. Next, expression (10) will be replaced into (5), imposing also the limit frequency−division condition $V \to 0$. Solving for E_{in}, one obtains a single real equation governing the circuit behavior at the division threshold:

$$E_{ino} = V_{2o}(L,\omega_{in})\left\{\left[1 - (Lc_o\omega_{in}^2 - 2c_o/c_c)\right]^2 + (R_pc_o\omega_{in})^2\right\}^{1/2} \qquad (11)$$

where the subindex "o" indicates that the input voltage is calculated at the division threshold. As gathered from (11), the expression for the input−amplitude threshold is composed by two factors. The middle−point capacitor c_c only affects the second factor. Provided that the inductor L fulfils $L > 1/(c_o\omega_{in}^2)$, it will be possible to choose c_c so as to minimize the input−amplitude threshold. Indeed, the second factor in (11), composed by the addition of two squared terms, will achieve a minimum at the capacitor value:

$$c_{cm} = 2c_o/(Lc_o\omega_{in}^2 - 1) \qquad (12)$$

which will lead to the following expression for the input−amplitude threshold:

$$E_{ino} = V_{2o}(L,\omega_{in})R_pc_o\omega_{in} \qquad (13)$$

On the other hand, from inspection of (11), the threshold E_{ino} decreases with the amplitude $V_{2o}(L,\omega_{in})$, which has the following expression, derived from (10):

$$V_{2o}(L,\omega_{in}) = \frac{\sqrt{(2R_D)^2 + \left[2X_L - c_o\omega_{in}\left(R_D^2 + X_L^2\right)\right]^2}}{\omega_{in}b\left(R_D^2 + X_L^2\right)} \qquad (14)$$

where $X_L = L\omega_{in}/4$. The magnitude $V_{2o}(L,\omega_{in})$ will exhibit a minimum if the following condition is satisfied:

$$\frac{L/2}{b\left[R_D^2 + (L\omega_{in}/4)^2\right]} - \frac{c_o}{b} = 0 \qquad (15)$$

The above condition, fulfilled at the given frequency $\omega_{in,c}$, agrees with $V_{2o}\cos\phi_{2o} = 0$ in (10)(a). This condition enables an optimum operation of the diodes at the subharmonic frequency, as they behave as pure negative resistances, without any additional reactive component. The frequency $\omega_{in,c}$ agrees with center of the division band. Indeed, at constant L, and because of the second squaring

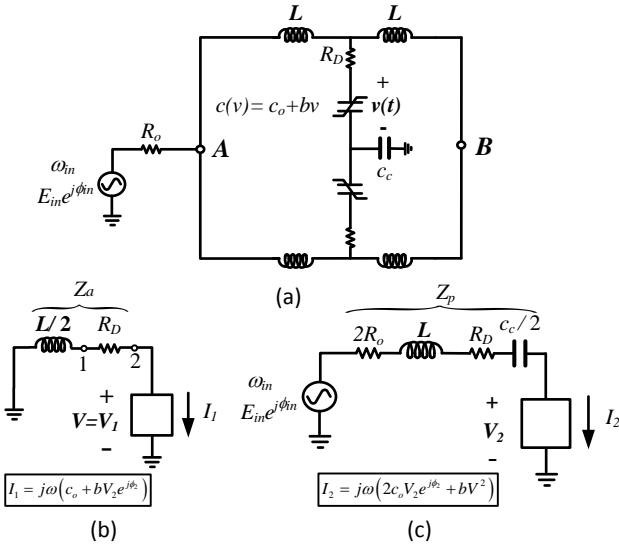operation under the root in (14), the frequency response will be nearly symmetrical about $\omega_{in,c}$.

Fig. 2 Single−cell frequency divider. (a) Full topology. (b) Equivalent circuit at the subharmonic frequency ω. (c) Equivalent circuit at the input frequency $\omega_{in} = 2\omega$.

For illustration, the varactor diode SMV1231 [15] has been considered. At the bias voltage $V_b = 0$ V, the parameters of the approximate model $c(v) = c_o + bv$ are $c_o = 1.88 \cdot 10^{-12}$ (F) and $b = 9.278 \cdot 10^{-13}$ (F/V). In a first design, the desired central frequency is $f_{in,c} = 2.15$ GHz. The inductor value L resulting from the condition (15) is $L_m = 23.3$ nH. The corresponding input−sensitivity curve is obtained with (11). As shown in Fig. 3, the inductor $L_m = 23.3$ nH centers the division band about $f_{in,c} = 2.15$ GHz for any c_c value. This inductor fulfils $L > 1/c_o \omega_{in}^2$, so it is possible to select the capacitor $c_{cm} = 2c_o / (Lc_o \omega_{in}^2 - 1) = 0.537$ pF that minimizes the input−amplitude threshold at $f_{in,c} = 2.15$ GHz. Due to the increased sensitivity with respect to the input signal under the resonance condition (12), the capacitor c_{cm} enables a broader division bandwidth (Fig. 3). This is studied in detail in Section C. As a second example, the same two−stage design method has been applied for a different central frequency $f_{in,c} = 1.79$ GHz, observing the same performance (Fig. 3).

The impact of the diode parameters c_o and b has also been analyzed. From a simple inspection of (10) the voltage amplitude $V_{2o}(L, \omega_{in})$ at the input frequency ω_{in} is inversely proportional to b, so according to (11) the input−amplitude threshold will decrease with b. On the other hand, the capacitance c_o affects (10)(a) and also the condition for a minimum in $V_{2o}(L, \omega_{in})$ given by (15). For a given L, a variation of c_o will shift the center of the division band, $\omega_{in,c}$, determined by (15). Provided that (12) is also fulfilled, a lower threshold will be obtained for smaller c_o, as gathered from (13). However, one should take into

account that both c_o and b depend on the particular bias voltage V_b of the varactor diode. In the case of the diode SMV1231 [15], both c_o and b decrease with V_b, in the whole V_b range, going from 0 V to 15 V. Fig. 4(a), presents the analysis of the input−amplitude threshold versus the inductor L, for different values of V_b. The lowest threshold is obtained for $V_b = 0$ V, providing the highest b. The impact of V_b on the input−sensitive curves is shown in Fig. 4(b). As expected, the lowest input−amplitude threshold and broadest division bandwidth is obtained for $V_b = 0$ V which will be the value considered in this work.
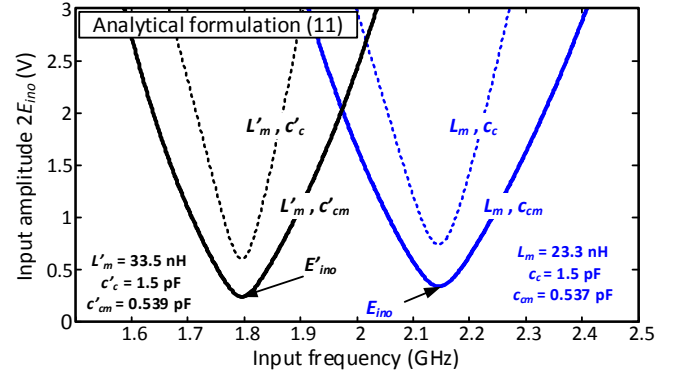

Fig. 3 Input−sensitivity curves for two different L_m values, centering the division band about two different frequencies. The input−amplitude values are referred to a positive−frequency spectrum ($2E_{ino}$). The sensitivity curves resulting for an optimum capacitor c_{cm} are traced in solid line in the two cases.
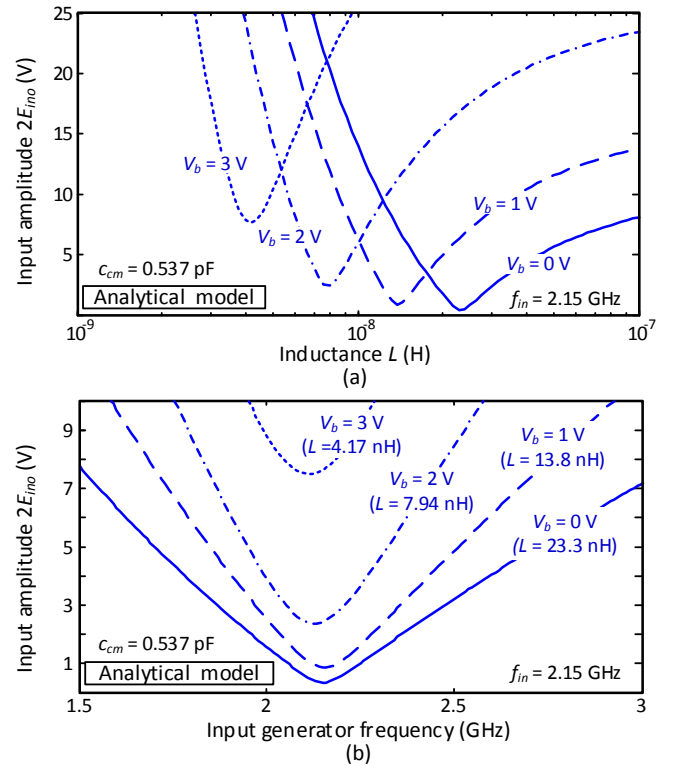

Fig. 4 Influence of the parameters of the diode model. (a) Variation of the input−amplitude threshold (in a positive−frequency spectrum) with the inductor L at the constant input frequency $f_{in} = 2.15$ GHz. (b)

Input−sensitivity curve with the bias voltage V_b, choosing, in each case, the inductor value that provides the minimum input−amplitude threshold at $f_{in} = 2.15$ GHz .

B. Multi−cell divider

A multi−cell divider, such as the one considered in Fig. 1(a), will be investigated. Initially, the study will be carried out using the model $c(v) = c_o + bv$ at the two frequencies $\omega_{in}/2$ and ω_{in}. The frequency−division condition (8) can be generalized to a multi−cell divider, which is done by means of an equivalent circuit analogous to the one in Fig. 2(b). The circuit total admittance is calculated at the node located between the first inductor and the rest of the varactor−inductor structure, at the subharmonic frequency ω. This provides the following recursive equation:

$$\frac{1}{jL\omega} + Y_1(1) + \left(jL\omega + \cfrac{1}{Y_1(2) + \cfrac{1}{jL\omega + \cfrac{1}{Y_1(3) + \cfrac{1}{jL\omega + ...}}}} \right)^{-1} = 0$$

(16)

where $Y_1(n)$, with $n = 1$ to N, are the diode subharmonic admittance functions and N is the number of back−to−back varactor pairs existing in the multi−cell divider, indexed as shown in Fig. 1(a). The admittance functions $Y_1(n)$ are defined as:

$$Y_1(n) = \frac{1}{R_D + \left(j\omega c_o + j\omega b \bar{V}_2(n) \right)^{-1}} \qquad (17)$$

Note that for $N = 1$, one has $Y_1(1) \equiv Y_1$ [see (7)−(9)]. In the above expression $\bar{V}_2(n)$ is the voltage component at ω_{in} across the nonlinear capacitor n. The bar stresses the fact that it is a complex magnitude. Equation (16) agrees with the flip bifurcation condition of the multi-cell divider. Combining (17) with (16), one obtains a complex equation of the form:

$$Y_T \left(\bar{V}_2(1), \ldots, \bar{V}_2(n), \ldots, \bar{V}_2(N), c_o, b, L, \omega \right) = 0 \qquad (18)$$

which depends on the whole set of second harmonic voltages $\bar{V}_2(n)$ at ω_{in}, calculated under the limit condition for frequency division $V \to 0$. These voltages provide the negative resistances that should compensate the passive impedances exhibited by the circuit at $\omega_{in}/2$, depending only on c_o, b and L. Using the first−order capacitance model and the two analysis frequencies $\omega_{in}/2$ and ω_{in} under the condition $V \to 0$, the phasors $\bar{V}_2(n)$ will depend linearly on the input voltage $E_{in}e^{j\phi_{in}}$, since the diode capacitance at ω_{in} is simply c_o. A different expression will exist for each phasor, having the general form:

$$\bar{V}_2(n) = A_n(c_c, c_o, L, 2\omega) \, E_{in}e^{j\phi_{in}} \qquad (19)$$

The replacement of (19) in (16) provides a complex nonlinear equation in E_{in} and ϕ_{in}, which can only be accurately resolved in a numerical manner. Because the flip−bifurcation (18) does not explicitly depend on c_c, one may expect a behaviour analogous to that of a single cell, regarding the two design parameters L and c_c. That is, the variation of L will shift the division band and the variation of c_c will modify the sensitivity to the input signal and, therefore, the division threshold. However, as gathered from (16), the optimum values of L and c_c for a desired central frequency $\omega_{in,c}$ will depend on the number of cells and should be optimized for each N. Note that when implementing a multi−cell configuration, divisions by higher order will not be usually observed, due to the loading effects of the L−varactor cells, which are tuned for frequency division by 2, instead of higher order divisions

Initially, a multi−cell divider with $N = 5$ back−to−back varactor pairs will be analyzed [Fig. 1(a) and (b)], as this is the same number considered in [1]-[2]. The impact of the number of N will be studied later in this section. For a realistic analysis and design, harmonic balance (HB) is used, together with an auxiliary generator (AG) [6]-[7]. The AG is needed because HB does not enable a direct optimization of frequency dividers. Even when setting the fundamental frequency to $\omega_{in}/2$, the HB simulation will converge by default to a solution with zero value at all the odd harmonics of $\omega_{in}/2$, since it contains a homogeneous subsystem at these frequency components [7]. The use of an AG at $\omega_{AG} = \omega_{in}/2$ prevents this default convergence [6]-[7]. The voltage AG is connected in parallel at a sensitive location, for instance between the nodes of a varactor diode in one of the innermost divider cells [Fig. 1(c)]. It contains an ideal bandpass filter centered at $\omega_{in}/2$, to avoid any influence at frequencies different from $\omega_{in}/2$. Due to the rational relationship with the input frequency, both the AG amplitude and its phase [or the phase of the input source] must be calculated in order to fulfil a non−perturbation condition. This condition is given by the zero value of the ratio between the AG current and voltage at $\omega_{in}/2$, expressed as $Y_{AG}(A_{AG}, \phi_{in}) = 0$, where the phase origin is taken between the AG terminals. In commercial HB, this condition is solved through optimization, with the pure HB system, with as many harmonics as desired, as an inner tier. After convergence, the voltage component at $\omega_{in}/2$, between the AG nodes, will agree with the AG value. Using this property, the division boundary will be obtained by setting the AG amplitude to a very small value $A_{AG} = \varepsilon$.

Taking into account the insight provided by the analytical study, the optimization procedure will be the one indicated in the flowchart of Fig. 5. It will start with the calculation of the inductor L that minimizes the input−amplitude threshold at the desired central frequency $\omega_{in,c}$. This is done by doing $\omega_{AG} = \omega_{in,c}/2$ and solving:

$$Y_{AG}(E_{in}, L, \phi_{in}) = 0 \qquad (20)$$

under the condition: $A_{AG} = \varepsilon$. Note that (20) is equivalent to the equation (18) of the simplified formulation. Because

equation (20) is complex, it contains two real equations in three unknowns, which provides a curve in the plane defined by L and E_{in}. To center the division band, L is swept, solving the complex equation (20) in terms of E_{in}, ϕ_{in} at each L step. The L value providing the minimum E_{in} is chosen. For illustration, the method will be applied to the divider shown in Fig. 1(a). In all the HB analyses presented hereafter, full diode models (including parasitics) and $NH = 20$ harmonic terms will be considered. The model used for the varactor diode SMV1231 is the one provided by the manufacturer [15]. Fig. 6(a) presents the results obtained when setting the AG frequency to the desired central value of the division band: $f_{AG} = f_{in,c}/2$, where $f_{in,c} = 2.15$ GHz. Three different values of c_c have been considered, but the inductor $L_m = 6.15$ nH provides the minimum E_{in} in the three cases, in agreement with the analytical study of the single cell. Next, the inductor is kept fixed at $L_m = 6.15$ nH, performing a sweep in the capacitor c_c and solving $Y_{AG}(E_{in}, \phi_{in}) = 0$ at each sweep step (Fig. 5). The minimum is obtained for $c_{cm} = 6.5$ pF [Fig. 6(b)]. The effect of varying the two parameters L and c_c on the bandwidth is analyzed by tracing the input−sensitivity curve in the plane defined by ω_{in} and E_{in}. The frequency ω_{in} is swept, solving the complex equation $Y_{AG}(E_{in}, \omega_{in}, \phi_{in}) = 0$ in terms of E_{in}, ϕ_{in} at each sweep step. Fig. 6(c) shows the sensitivity curves obtained for different pairs of values L, c_c. For each L value, the sensitivity curve gests centered about a different frequency ω_{in}. Once the divider is centered about the desired frequency $\omega_{in,c}$, the capacitor c_c can be used to reduce the input−amplitude threshold. In agreement with the analytical study, variations of this capacitor do not shift the operation band.
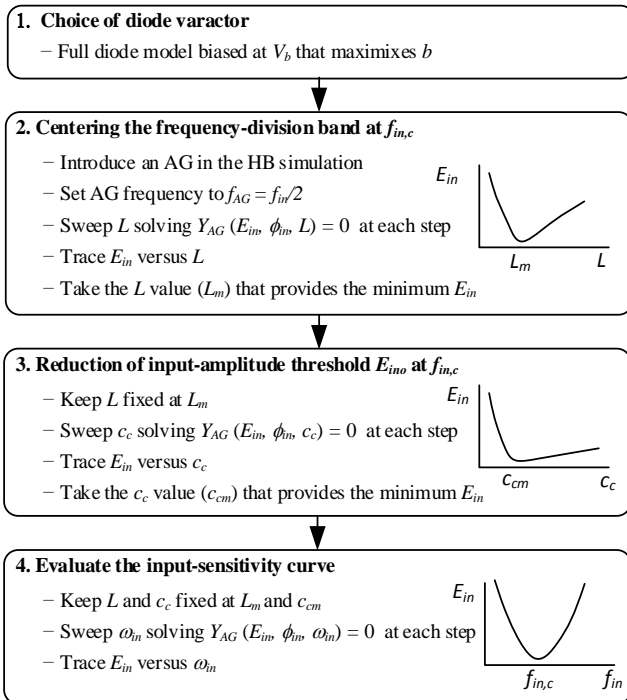
The sketch and picture of the measurement set−up are shown in Fig. 7. It is based on the use of the Agilent 90804A Digital Storage Oscilloscope and the E4446A PSA spectrum analyzer (with phase noise measurement personality). The circuit is injected using the Rhode & Schwarz SMT06 signal generator. In this particular case, the divided solutions have been measured with two Agilent 1134A differential probes, which enable flexibility to test the differential waveforms at various circuit nodes. Measurement points have been superimposed in Fig. 6(a) to Fig. 6(b) with good agreement.
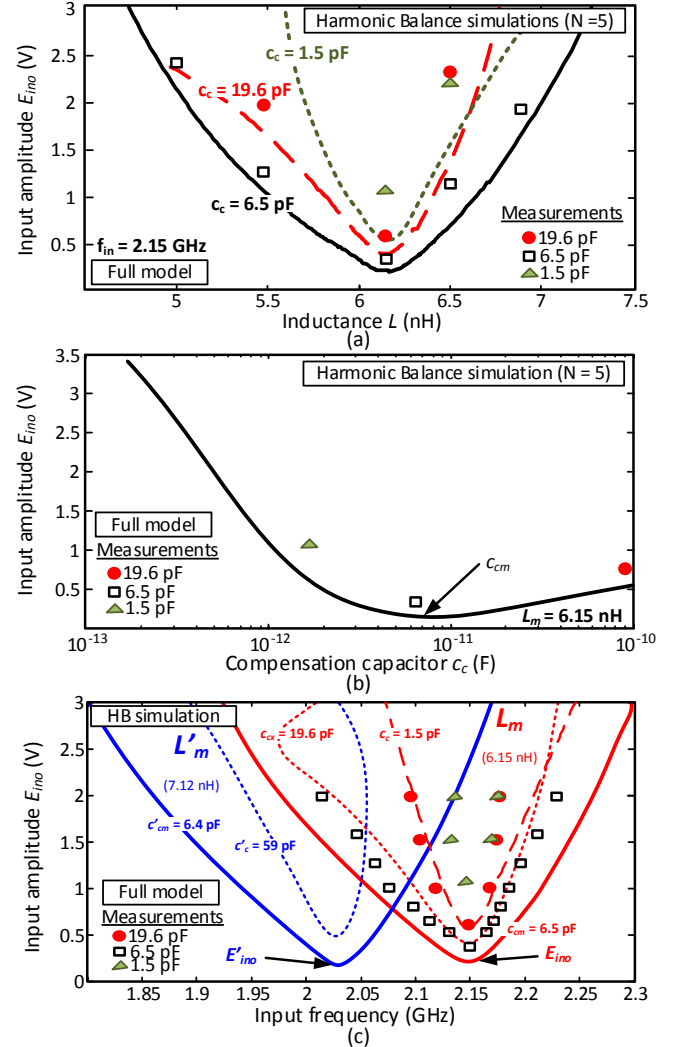

Fig. 6 Optimization of the multi−cell divider based on the diode SMV1231 in Fig. 1(a) by means of HB−AG simulations with $NH = 20$ harmonic terms. (a) Selection of the inductor value that minimizes the input−amplitude threshold at the desired central frequency $f_{in} = 2.15$ GHz. (b) Further minimization through a proper selection of the additional capacitor c_c. (c) Input−sensitivity curves for the optimum inductor $L_m = 6.15$ nH at $f_{in} = 2.15$ GHz and for a different inductor value, which centers the band about $f_{in} = 2.027$ GHz. In each case, the input−amplitude threshold is minimized through an independent analysis versus c_c.

1. **Choice of diode varactor**
   − Full diode model biased at V_b that maximixes b

2. **Centering the frequency-division band at $f_{in,c}$**
   − Introduce an AG in the HB simulation
   − Set AG frequency to $f_{AG} = f_{in}/2$
   − Sweep L solving $Y_{AG}(E_{in}, \phi_{in}, L) = 0$ at each step
   − Trace E_{in} versus L
   − Take the L value (L_m) that provides the minimum E_{in}

3. **Reduction of input-amplitude threshold E_{ino} at $f_{in,c}$**
   − Keep L fixed at L_m
   − Sweep c_c solving $Y_{AG}(E_{in}, \phi_{in}, c_c) = 0$ at each step
   − Trace E_{in} versus c_c
   − Take the c_c value (c_{cm}) that provides the minimum E_{in}

4. **Evaluate the input-sensitivity curve**
   − Keep L and c_c fixed at L_m and c_{cm}
   − Sweep ω_{in} solving $Y_{AG}(E_{in}, \phi_{in}, \omega_{in}) = 0$ at each step
   − Trace E_{in} versus ω_{in}

Fig. 5 Flowchart indicating the steps to be taken for the optimized design of the frequency divider.

Now the impact of the inductor−varactor cells will be investigated. Initially, the first−order model $c(v) = c_o + bv$ has been considered. The central frequency is set to $f_{in,c} = 2.15$ GHz. Then the inductor L that minimizes the input−amplitude threshold at $f_{in,c} = 2.15$ GHz is calculated numerically using the flip−bifurcation condition (18) for different N values. Fig. 8(a) presents the resulting

input−sensitive curves. A different L is obtained for each N, but the division band is centered about $f_{in,c}$ in all cases. For each N, the division threshold is further reduced through a proper selection of the capacitor c_c, as shown in Fig. 8(a). Fig. 8(b) presents the same analysis, using the HB−AG method with full diode models and $NH = 20$ harmonic terms. Each sensitivity curve corresponds to the L and c_c obtained following the flowchart of Fig. 5. As expected, for moderate input−amplitude levels, there is very good agreement between the results obtained with (16) and with HB.
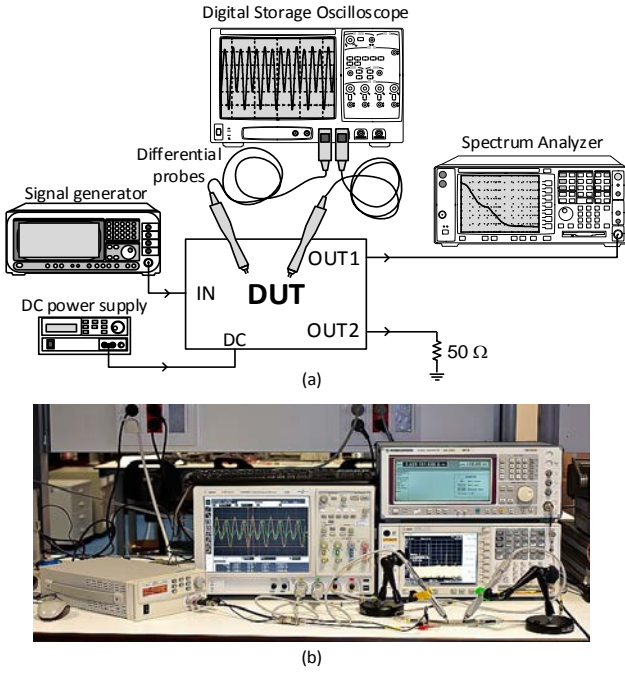

Fig. 7 Measurement test−bench. (a) Sketch. (b) Photograph.

As shown in Fig. 8(a) and Fig. 8(b), there is a reduction of the division bandwidth when increasing N. To investigate this effect, the variation of ϕ_{in} through the flip−bifurcation loci obtained for different N has been analyzed in Fig. 8(c). The phase−shift interval with high sensitivity to ω_{in} decreases with N, which is due to an earlier saturation effect in the nonlinear function in ω_{in} that governs the phase shift dependence: $\phi_{in}(\omega_{in})$. Therefore, for given input amplitude, the fulfillment of the resonance condition at $\omega_{in} / 2$, required for the frequency division, is limited to a smaller ω_{in} interval. Despite this reduction of the frequency band, the increase in N can be interesting for certain applications, since it enables higher subharmonic amplitude through the divider circuit, as was demonstrated in [9]. Indeed, for a higher N, the subharmonic gain increases [1]-[2] due to the cooperative effect of more varactor diodes. This is demonstrated in Fig. 9, which compares the resonance near the subharmonic frequency, responsible for the frequency division by 2, for different N values. As can be seen, a more negative conductance (responsible for the subharmonic amplification) is obtained for higher N. The higher frequency selectivity is also noted, in consistency with Fig. 8(c).
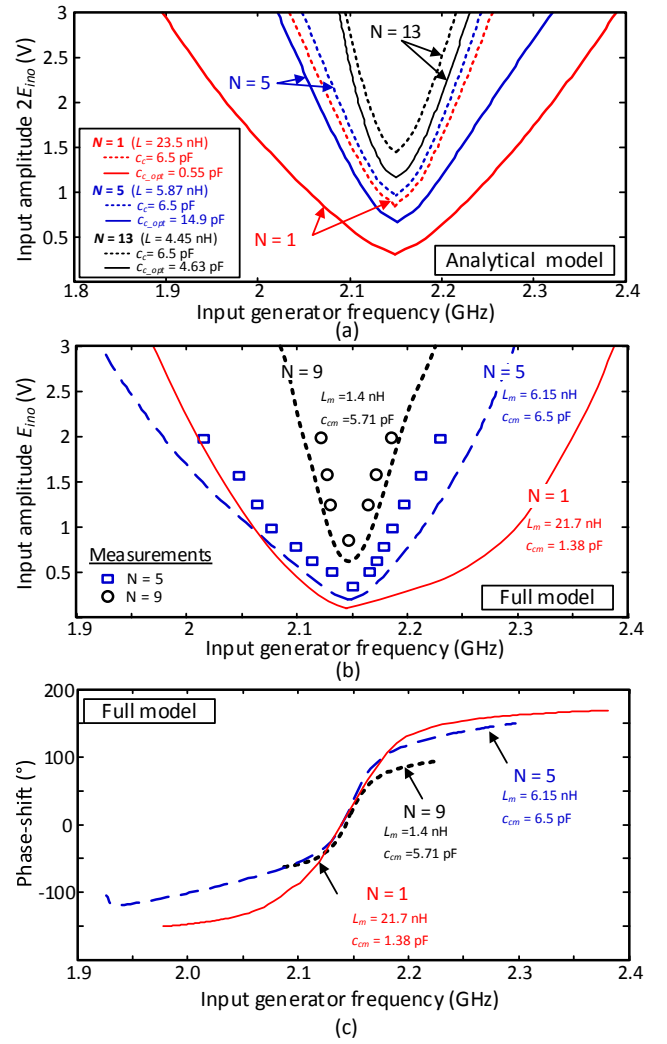

Fig. 8 Influence of the number N of back−to−back diode pairs on the frequency−division band. (a) Through the numerical solution of (16), based on a first−order model of the diode. (b) Using the HB−AG method with full diode models and $NH = 20$ harmonic terms. (c) Variation of the phase shift between the input source and the subharmonic voltage through the flip−bifurcation loci in (b).
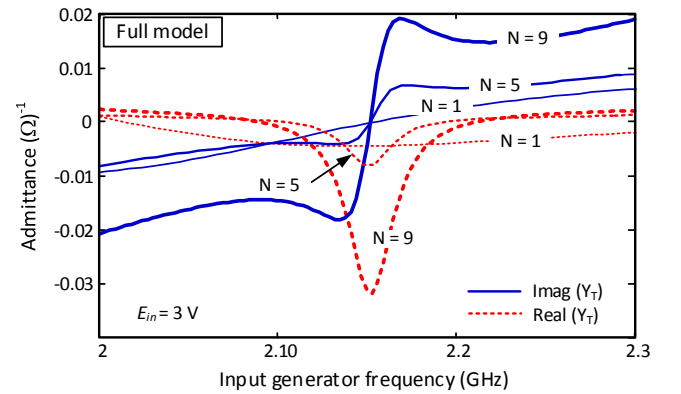

Fig. 9 Resonance near the subharmonic frequency, responsible for the frequency division by 2, for different N values. A more negative conductance (responsible for the subharmonic amplification) is obtained for higher N.

C. Frequency bandwidth

The analysis of the frequency bandwidth will initially be carried out using the analytical expression (11), valid for

one cell. Then the multi−cell divider with $N = 5$ diode pairs will be studied with the HB−AG method. The impact of the additional capacitor c_c is analyzed solving (11) for c_c, in terms of E_{in}, ω_{in} and L, which provides:

$$c_c = \frac{2c_o}{Lc_o\omega_{in}^2 - 1 \pm \sqrt{\left(E_{in}/V_{2o}(L,\omega_{in})\right)^2 - R_p^2 c_o^2 \omega_{in}^2}} \qquad (21)$$

Sweeping ω_{in} at constant E_{in} and L, two different curves are obtained, respectively corresponding to the positive and negative sign before the root operation. In Fig. 10(a), the two curves have been traced (in solid and dashed lines) for different E_{in} values and the inductor L_m resulting from the minimization of the input−amplitude threshold at $f_{in,c} = 2.15\,\text{GHz}$. Division by two is obtained inside the region delimited by the two curves. For each E_{in}, the edges of the maximum frequency bandwidth are given by the condition $[E_{in}/V_{2o}(L,\omega_{in})]^2 - R_p^2 c_o^2 \omega_{in}^2 = 0$ in (21), which is satisfied for a different ω_{in} at each side, due to the frequency dependence of $V_{2o}(L,\omega_{in})$. The curve c_c vs. ω_{in} exhibits an infinite slope at each of the two points fulfilling that condition.

When setting the input amplitude to the global minimum $Min(E_{ino})$ at $f_{in,c} = 2.15\,\text{GHz}$, the two infinite slope points merge into a single one and solution curve degenerates into a point, obtained for the optimum capacitor value c_{cm} [see (7)]. As E_{in} increases from this value, the two sections in (21) form a closed curve that later becomes an open curve. This is because for large E_{in}, the minus sign before the denominator root gives rise to a (discarded) negative capacitor. As shown in Fig. 10(a), below certain c_c value division is no longer possible, due to insufficient subharmonic gain of the nonlinear capacitances. On the other hand, for too large c_c, this capacitor no longer has an impact on the divider operation, which justifies the open curves in the representation of Fig. 10(a).

For a particular capacitor value c_{cx}, there is a constant−E_{in} curve such that its upper section is tangent to the straight line $c_c = c_{cx}$ [Fig. 10(a)]. The particular E_{in} value of this curve corresponds to the minimum threshold E_{ino} in the plane (ω_{in}, E_{in}). On the other hand, the capacitor values providing the maximum frequency excursion for each E_{in} do not differ too much [Fig. 10(a)]. The maximum bandwidth is obtained for a c_c value that approximates the one resulting from the threshold−minimization procedure in Section A, for which a single point is obtained in the representation of Fig. 10(a), indicated as $Min(E_{ino})$. Therefore, the minimization of the division threshold at a particular frequency $\omega_{in,c}$ should also enable a near maximum frequency bandwidth.
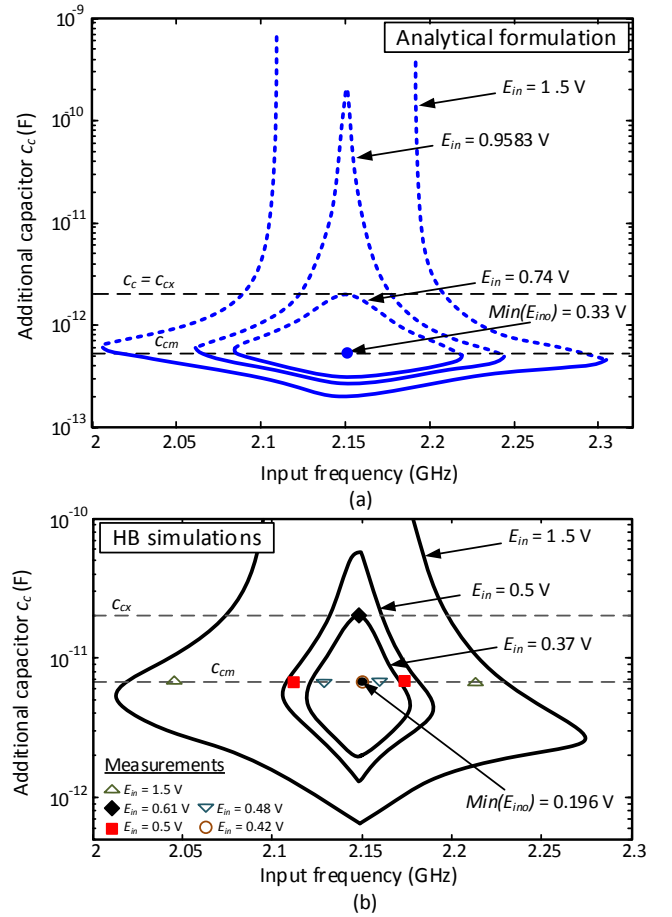

Fig. 10 Variation of the frequency bandwidth with the additional capacitor c_c for different values of the input amplitude E_{in}. (a) Analytical calculation. Frequency division is obtained inside each curve or pair of curves resulting from (21). (b) HB−AG analysis of the multi−cell divider with $N = 5$ diode pairs cell divider in Fig. 1. Measurements have been superimposed.

The above analytical results have been validated in the multi−cell divider with $N = 5$ diode pairs [Fig. 1(a)], using a HB simulation with $NH = 20$ harmonic terms. The frequency division loci have been traced in the plane defined by ω_{in}, c_c for several E_{in} values [Fig. 10(a)]. Each locus is obtained by solving the equation $Y_{AG}(\phi_{in}, c_c, \omega_{in}) = 0$. The analysis have been carried out for the optimum inductor value $L_m = 6.15\,\text{nH}$, resulting from the simulation in Fig. 6(a). In good qualitative agreement with the analytical formulation, the division band degenerates to a point when E_{in} is fixed to the global minimum input−amplitude threshold [Fig. 10(b)]. The corresponding c_c value agrees with the one providing the minimum E_{in} when sweeping c_c at constant $L_m = 6.15\,\text{nH}$. Measurements are superimposed.

D. *Phase noise*

Phase noise is a relevant characteristic of the frequency−divided solution. To calculate this solution at given input amplitude E_{in} and frequency ω_{in}, one should solve the non−perturbation condition in terms of the AG amplitude and input phase, $Y_{AG}(\phi_{in}, A_{AG}) = 0$, as done in [10]. Once the non−perturbation condition is fulfilled, the voltage at the subharmonic frequency $\omega_{in}/2$ agrees with the AG voltage at the connection nodes, so one can write

$V_1 = A_{AG}$. For an understanding of the phase−noise behavior, the outer−tier function $Y_{AG}(\phi_{in}, A_{AG})$ will be linearized about the divided steady−state solution in the presence of noise sources. The AG, which uses the pure HB system as an inner tier, enables control of the subharmonic voltage, so the partial derivatives with respect to V, ϕ_{in} and ω, denoted as Y_V, Y_ϕ and Y_ω, can be calculated through finite differences [8], [16]. The partial derivative Y_V is obtained through increments in A_{AG}, while keeping the frequency and phase constant at their original values, ω_{ino}, ϕ_{ino}, the ones fulfilling $Y_{AG}(A_{AGo}, \phi_{ino}) = 0$. In turn, the partial derivative Y_ϕ is obtained through increments in ϕ_{in}, while keeping the frequency and amplitude constant at their original values, ω_{ino}, A_{AGo}. An analogous procedure is carried out to calculate Y_ω.

In the phase−noise analysis, amplitude noise from the input source will be neglected, considering only the input phase noise $\psi(t)$. The phase noise of a divider by M is expected to follow $\psi(t)/M$ up to a certain offset frequency, usually beyond the region of influence of the circuit flicker noise. Thus, only white−noise sources will be considered. The circuit contains several white noise sources but they will all be modeled with a single equivalent current noise source. An example of the derivation of this kind of model is presented in [8]. The complex equivalent noise source, denoted as $I_N(t)$, is connected in parallel with the AG [8].

Taking into account the effect of the circuit noise sources, the total phase perturbation the observation node can be expressed as $\Delta\phi_T = \psi(t)/2 + \Delta\phi(t)$ [8], [17]. In turn, the subharmonic amplitude undergoes an increment $\Delta V(t)$ with respect to the steady−state value V_1. The time−varying phase and amplitude gives rise to an instantaneous complex frequency that can be expressed [8], [17]:

$$\dot{\varphi}(t) = \omega_{in/2} + \left(\frac{\dot{\psi}}{2} + \Delta\dot{\phi}\right) - j\frac{\Delta\dot{V}}{V_1} \qquad (22)$$

Then the phase−noise spectral density can be estimated with the following expression, derived in [7]−[8]:

$$\left|\Delta\phi_T(\Omega)\right|^2 = \frac{\left|Y_V \times Y_\phi\right|^2 \dfrac{\left|\psi(\Omega)\right|^2}{4} + 2\left|Y_V\right|^2 \dfrac{\left|I_N\right|^2}{V_1^2}}{\left|Y_V \times Y_\phi\right|^2 + \left|Y_V \times Y_\omega\right|^2 \Omega^2} \qquad (23)$$

where $\times$ indicates the cross product between real and imaginary parts. The varactor based divider will usually exhibit low frequency sensitivity, so it will be possible to approach the above equation with:

$$\left|\Delta\phi_T(\Omega)\right|^2 = \frac{\left|\psi(\Omega)\right|^2}{4} + \frac{2}{\left|Y_\phi\right|^2 V_1^2 \sin^2(\alpha_\phi - \alpha_V)}\left|I_N\right|^2 \qquad (24)$$

where α_ϕ is the angle of Y_ϕ and α_V is the angle of Y_V.

For low frequency sensitivity, the divider will follow the divided phase noise of the input source up to certain offset frequency, from which the circuit white noise sources will dominate. This will give rise to a transition from a spectrum closely following that of the input source to a flat spectrum. The transition will occur at the offset frequency Ω_0 for which the two terms in (24) have an identical magnitude. Assuming a low noise input source, the frequency Ω_0 will be larger for a higher magnitude $\left|Y_\phi\right|$, since this means a higher sensitivity to the phase of the input source. It will also decrease with the subharmonic amplitude V_1 and for angles $\alpha_\phi - \alpha_V$ close to an odd multiple of $\pi/2$.

The above conclusions have been validated with a detailed phase−noise analysis based on the conversion−matrix approach [18]−[19] and with measurements. For the analysis with the conversion−matrix approach, the circuit is linearized about the periodic regime obtained with the AG, which is provided as an initial guess to the large−signal small−signal analysis of the commercial software. The analyses have been performed for several input frequencies, comparing the offset frequencies Ω_0 and the denominator of the second term of (14) in Table I. In Fig. 11, the phase−noise spectrum of the subharmonic component, extracted with an impedance transformer, is compared with the spectrum of the input source.
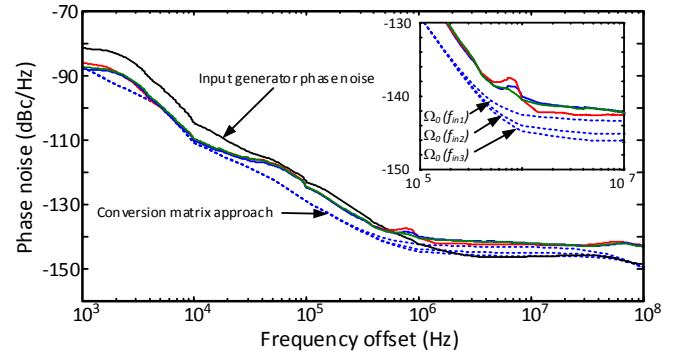

Fig. 11 Phase−noise analysis of the multi−cell divider with $N = 5$ diode pairs. Comparison between the phase noise spectra obtained with the approximate expression (24) and with the conversion−matrix approach. Measurements have been superimposed.

TABLE I – PHASE NOISE CORNER FREQUENCY

Input frequency f_{in} (GHz)	$\left|\bar{Y}_\phi\right|^2 V_1^2 \sin^2(\alpha_\phi - \alpha_V)$	Frequency corner Ω_0 (kHz)
$f_{in1} = 2.20$	$4.182 \cdot 10^{-10}$	450
$f_{in2} = 2.15$	$5.714 \cdot 10^{-10}$	520
$f_{in3} = 2.10$	$1.371 \cdot 10^{-9}$	700

III. DUAL−PHASE DIVIDER

The use of two frequency dividers based on differential varactor−inductor cells, together with a balun, should enable the implementation of a dual−phase divider, with application in the generation of in−phase and quadrature signals [12], [20]. A planar Marchand balun [11] will be used here, which is based on two sections of coupled transmission lines, having an electrical length of 180° at the

central operation frequency ω_{inc}, as shown in Fig. 12. Initially, an analytical study of the configuration will be performed, using single−cell dividers [Fig. 12(a)]. Next, the practical case of a multi−cell divider with $N = 5$ diode pairs will be studied [Fig. 12(b)−(c)], by means of numerical simulations and measurements.

In the simpler case of ideal transmission lines, the admittance matrix describing the Marchand balun at $\omega_{in,c}$ is the following:

$$\begin{bmatrix} \bar{I}_{in} \\ \bar{I}_a \\ \bar{I}_b \end{bmatrix} = \begin{bmatrix} 0 & -j\gamma & j\gamma \\ -j\gamma & 0 & 0 \\ j\gamma & 0 & 0 \end{bmatrix} \begin{bmatrix} \bar{V}_{in} \\ \bar{V}_a \\ \bar{V}_b \end{bmatrix} \quad (25)$$

where the currents and voltages at the three ports are defined as shown in Fig. 12(a). For generality, we will consider different voltage and current values at the inputs of the two dividers. This will be the case if one of the dividers is detuned with respect to the other. The analysis as a phase shifter requires full consideration of the nonlinear behavior with respect to the subharmonic components, so the components of the diode current will be given by (2), with $V \neq 0$.

The matrix (25) provides the following relationships at the input frequency ω_{in}:

$$\begin{aligned} I_{in} &= -j\gamma V_a + j\gamma V_b & (a) \\ I_a &= -j\gamma V_{in} = -I_2 & (b) \\ I_b &= j\gamma V_{in} = -I_2 \text{'} & (c) \end{aligned} \quad (26)$$

where the *prima* indicates variables referring to Divider B in Fig. 12. At the subharmonic frequency, each divider is terminated in virtual short circuits, so their individual subharmonic components fulfill:

$$\begin{aligned} V_1 + Z_a \bar{I}_1 &= 0 & (a) \\ \bar{V}_1 \text{'} + Z_a \bar{I}_1 \text{'} &= 0 & (b) \end{aligned} \quad (27)$$

where Z_a corresponds to the same impedance already defined in (4). Note that the phase origin is taken at the subharmonic component of the voltage across the varactor diode in the Divider A, so $\bar{V}_1 \text{'}$ is a phasor of the form: $\bar{V}_1 \text{'} = V_1 \text{'} e^{j\phi_1}$. Applying Kirchoff's laws at the input frequency ω_{in}, under consideration of (26)(b) and (26)(c), one obtains:

$$\begin{aligned} E_{in} - \frac{I_2}{j\gamma} &= R_0 I_{in} & (a) \\ E_{in} + \frac{I_2 \text{'}}{j\gamma} &= R_0 I_{in} & (b) \end{aligned} \quad (28)$$

Replacing alternatively (28)(a) and (28)(b) into (26)(a), the following equations are derived:

$$G_0 \bar{E}_{in} = j\left[\frac{2G_0}{\gamma} + 2\gamma Z\right]\bar{I}_2(V_1, \bar{V}_2) + j\gamma\left(\bar{V}_2 - \bar{V}_2\text{'}\right)$$

$$G_0 \bar{E}_{in} = -j\left[\frac{G_0}{\gamma} + 2\gamma Z\right]\bar{I}_2\text{'}(\bar{V}_1\text{'}, \bar{V}_2\text{'}) + j\gamma\left(\bar{V}_2 - \bar{V}_2\text{'}\right) \quad (29)$$

where $G_o = 1 / R_o$ and $Z = jL\omega_{in} - j2/(c_c \omega_{in})$. The difference between the voltage and current values at the two diodes is due to their different bias voltages. In the approximate model (29) each divider is coupled to the other only at the input frequency ω_{in}.
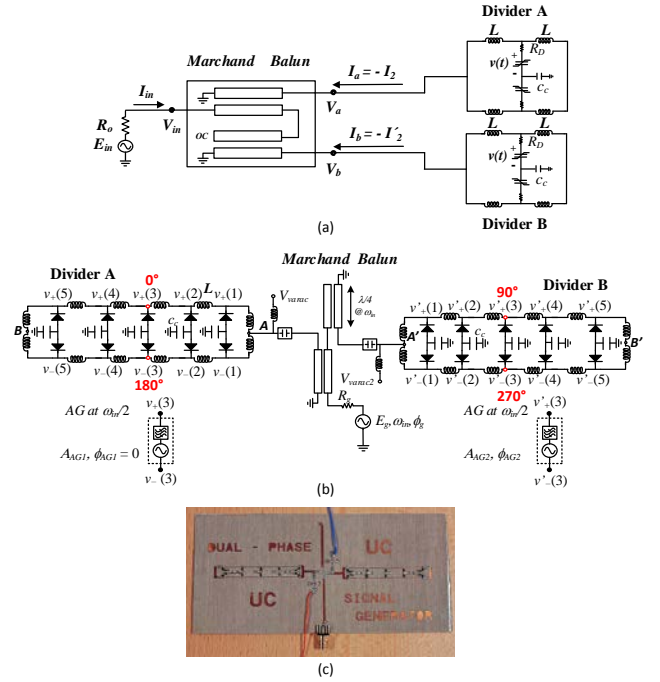

(a)

(b)

(c)

Fig. 12 Dual−phase signal generator based on two varactor−based frequency dividers, connected through a Marchand balun. (a) Currents and voltages at the three ports of the Marchand balun. (b) Schematic. (c) Photograph of the prototype built in Rogers 4003C substrate $\left(\varepsilon_r = 3.38, \ H = 0.508 \text{ mm}\right)$.

To analyze the phase shifting capabilities, one should determine the phase of the subharmonic voltage $\bar{V}_1 \text{'} = V_1 \text{'} e^{j\phi_1}$ since the phase of $\bar{V}_1$ is zero. The two nonlinear equations in (29) can only be resolved numerically, but they can provide an intuition on the impact of $\bar{V}_2$ on the phase shift. With this aim, the diode in Divider A is modeled with c_o, b. In turn the diode in Divider B, undergoing the biasing variations, is modeled with $c_o\text{'}, b\text{'}$. For a rough analysis of the impact of the coupling effects, one can define an equivalent current source:

$$\bar{I}_{in}^T = G_0 \bar{E}_{in} + j\gamma \bar{V}_2 \quad (30)$$

And solving (29)(b) for $\bar{V}_2 \text{'}$ one obtains:

$$\bar{V}_2 \text{'} = \frac{\bar{I}_{in}^T - \alpha b\text{'} \bar{V}_1 \text{'}^2}{\beta c_0 \text{'} + j\gamma} \quad (31)$$

where the following parameters with frequency dimension have been introduced $\alpha = 4G_o\omega / \gamma + 8\gamma\omega Z$ and

$\beta = 2G_o \omega / \gamma + 4\gamma\omega Z$. Expression (31) will be replaced into (27)(b) considering the capacitance model $c(v) = c_o\,' + b\,'v$ to obtain the current component $\overline{I}_1\,'$. This leads to:

$$1 + j\omega Z_a \left[c_0\,' + b\,' \frac{\overline{I}_{in}^{\,T} e^{-j2\phi_1} - \alpha b\,' V_1\,'^2}{\beta c_0\,' + j\gamma} \right] = 0 \qquad (32)$$

At a constant $\omega_{in} = 2\omega$, all the impedance terms will be constant too, so varying the parameters $c_o\,', b\,'$ will necessary give rise to a variation in $V_1\,'$ and ϕ_1. From (26)(b) and (26)(c), one has $I_2 = -I_2\,'$, so it is possible to obtain the following relationship:

$$2c_o \overline{V}_2 + b V_1^2 = -2c_o\,' \overline{V}_2\,' - b\,' \overline{V}_1\,'^2 \qquad (33)$$

Because the biasing is varied in Divider B, one can expect the subharmonic amplitude to experience larger variations in this divider. Equation (33) indicates that the subharmonic oscillation may be extinguished in Divider B but not in the other, since, even when $\overline{V}_1\,' = 0$, this equation can provide $V_1 \neq 0$. Of course, this condition will delimit the operation interval. For same bias voltage in the two dividers, one will have $c_0 = c_0\,'$ and $b = b\,'$, and due to the circuit symmetry, equation (33) will provide the solution:

$$\overline{V}_1\,' = e^{j90} V_1, \qquad \overline{V}_2 = -\overline{V}_2\,' \qquad (34)$$

Then, the two dividers are ruled by a same equation:

$$G_0 \overline{E}_{in} = -j \left[\frac{2G_0}{\gamma} + 2\gamma Z \right] \overline{I}_2(V_1, \overline{V}_2) + j2\gamma \overline{V}_2 \qquad (35)$$

Due to the relationship (34), equivalent nodes of each divider will exhibit a 90° phase shift. This is indicated in Fig. 12(b). For instance, signals at the upper node of cell n in Divider B and at the upper node of the same cell n in divider A will exhibit a 90° phase shift. Signals at the lower node of cell n in Divider B and at the lower node of the same cell n in divider A will also exhibit a 90° phase shift. On the other hand, upper and lower nodes of any cell in any of the two dividers will exhibit a 180° phase shift.

Fig. 13 presents the numerical analysis of a dual−phase signal generator based on the use of two one−cell dividers. It shows the variation of the subharmonic amplitudes in the two dividers when changing the bias voltage of Divider B. The analysis demonstrates the coupling between the two dividers since the amplitude in Divider A varies with this bias voltage. A practical dual−phase generator based on two multi−cell dividers with $N = 5$ diode pairs has also been analyzed by means of two AGs, connected in a differential manner, at the central cell of each divider [Fig. 12(b)]. The amplitude variations are superimposed in Fig. 13 and exhibit the same qualitative behavior. In the two cases, the amplitude of Divider B undergoes the most significant variation, as this bias voltage directly affects the performance of the diodes in Divider B, whereas those in Divider A are affected by this bias voltage only through coupling effects. This gives rise to the amplitude imbalance observed in Fig. 13. With this hyperabrupt diode the

amplitude is quite sensitive to the varactor bias voltage, even in the case of a single (uncoupled) divider. The aim here is to present a proof of concept, though a more careful consideration of this aspect might be needed for some applications. In the case of the one−cell divider, the section comprised between the flip bifurcation F_2 and the turning point T of the divided solution curve is unstable, as has been verified with pole−zero identification [21]. In the V_b range (2.27 V − 2.48 V), both the non−divided solution and the divided one located in the upper section of the curve are stable. Therefore, the divider will exhibit a small hysteresis interval, which is a common phenomenon in frequency dividers [7].
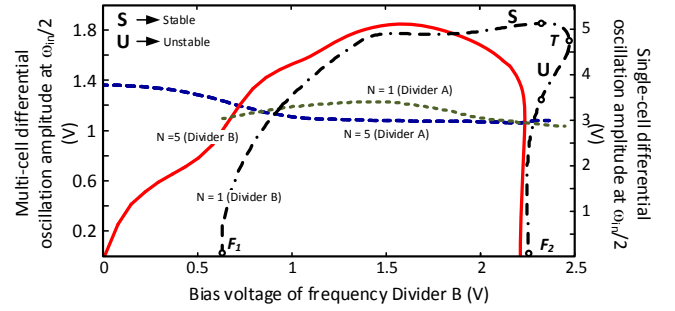
Fig. 13 Variation of the subharmonic amplitudes versus the reverse bias voltage applied to the varactors of Divider B. The cases of a single−cell divider and a multi−cell divider with $N = 5$ diode pairs are compared.

Fig. 14 presents the experimental waveforms between equivalent terminals of the two $N = 5$ dividers for two different values of the varactor bias voltage. Fig. 14(a) shows a phase shift of 90°, for equal bias voltages, and Fig. 14(b) shows a phase shift of 54°, under detuning. The measured variation of the phase shift with the varactor bias voltage is presented in Fig. 15. When increasing the reverse bias voltage in one of the dividers, the phase shift decreases, though there is a near flat region in the middle. This detuning could only be performed in one sense, since the original (equilibrium) operation point corresponds to near zero varactor−bias voltage.
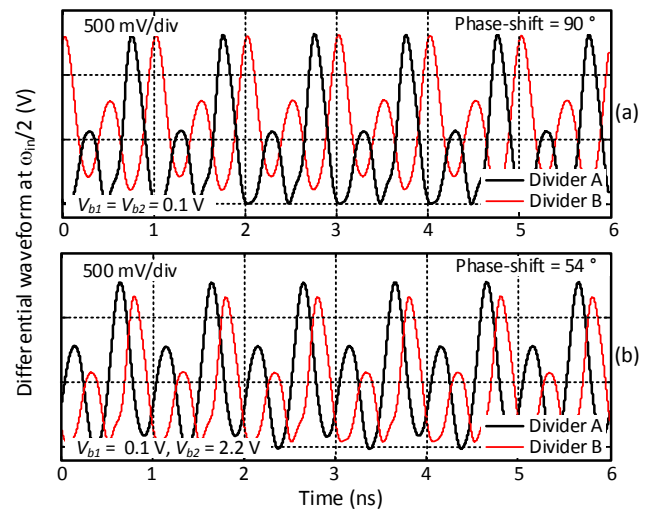
Fig. 14 Measured differential waveform for two different varactor bias voltages. (a) Phase shift 90° (b) Phase shift 54°.
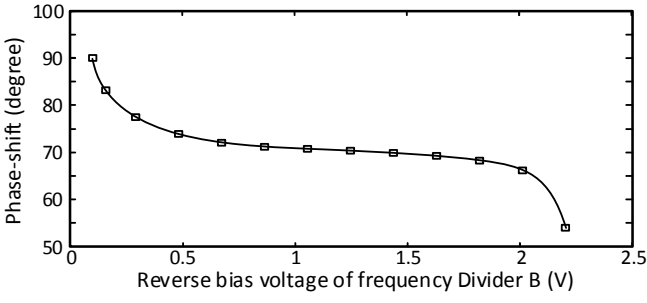
Fig. 15 Measured variation of the phase−shift between the two divider circuits with the reverse bias voltage applied to the varactors of Divider B.

IV. DUAL−BAND FREQUENCY DIVIDER

The possibility to implement a dual−band frequency divider using an extension of the reflective topology will be investigated in this section. This will rely on the combination of the original cell, based on the parallel connection of the varactor diode, with a series−varactor cell, in which the diodes are in a series connection (Fig. 16).

A. Series−varactor cell

Initially, an analytical study of the series−varactor cell (Fig. 16) will be carried out. Taking into account the symmetry properties of the structure, the nodes A and B will be virtual short circuits at the subharmonic frequency, in analogous manner to the case of the original cell. Thus, at $\omega = \omega_{in} / 2$ the circuit will be governed by the equation:

$$V + (R_D + j2L\omega)I_1 = V + Z_b I_1 = 0 \tag{36}$$

where $Z_b = R_D + j2L\omega$ and I_1 has the same expression as in (2). As gathered from the above equation, the dual cell exhibits an inductive effect which is four times that in the original cell (5). One obtains the same formal expression (14) for $V_{2o}(L,\omega_{in})$, though the definition of X_L is different and given by $X_L{'} = L\omega_{in}$. The different amplitude function will be emphasized with the notation $V_{2o}^{'}(L,\omega_{in})$. For a same L value the minimum of $V_{2o}^{'}(L,\omega_{in})$ will be obtained for a lower frequency than in the case of the original cell.
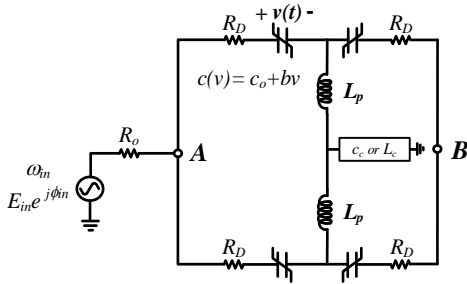

Fig. 16 Schematic of the series−varactor cell for frequency division at the lower band.

To reduce the division threshold at a particular input frequency $\omega_{in,c}$, one may choose an additional capacitive element c_c, as in the case of the parallel cell, or an additional inductive element L_c. In both cases, this additional element will be connected between the middle node of the parallel inductors and ground. In the case of a capacitive element c_c, the equation governing the divider at the division threshold $(V = 0)$ is the formally identical to (11), but replacing $V_{2o}(L,\omega_{in})$ with $V_{2o}^{'}(L,\omega_{in})$. In the case of an additional inductor L_c, the equation at the subharmonic component agrees with (36). However, the equation at the input frequency is different from (11). This equation, and the inductor L_c that minimizes the input−amplitude threshold for $L < 1/(c_o\omega_{in}^2)$ are given by:

$$E_{in} = V_{2o}^{'}(L,\omega_{in})\left\{\left[1-(L+2L_c)c_o\omega_{in}^2\right]^2 + (R_p c_o\omega_{in})^2\right\}^{1/2}$$
$$L_{cm} = 1/(2c_o\omega_{in}^2) - L/2 \tag{37}$$

For $L > 1/(c_o\omega_{in}^2)$, one should use an additional capacitor c_c.

B. Dual−band divider

The basic configuration of the dual−band divider consists of a series−varactor cell embedded between two parallel varactor cells, as shown in Fig. 18. In view of expressions (4) and (36), for given values of R_D, c_o and L, one can expect the parallel−varactor divider to operate at higher frequencies than the series−varactor one, due to the lower inductive effect. At these higher frequencies, the effect of the series−varactor cell will be initially neglected, since the impedances exhibited by its associated varactors and inductors will be low and high, respectively. Thus, in the higher frequency band, the configuration in Fig. 17 can be simplified as two parallel−varactor cells, responsible for the division at the higher frequency band. Their inductor L and additional capacitor c_c have been optimized according to the procedure described in Section II, imposing the central frequency $f_{in} = 3.97$ GHz. The optimum values resulting from a HB−AG simulation with full diode models and $NH = 20$ harmonic terms are $L_m = 4.7$ nH and $c_{cm} = 0.43$ pF.

Next, the lower frequency division band will be considered. It is initially assumed that the components of two outermost cells can be neglected at this low frequency, so the circuit in Fig. 17 simplifies to a single series−varactor cell. For this single cell, the inductor is kept at $L_m = 4.7$ nH, which centers the lower division band at $f_{in} = 1.72$ GHz. Then the analytical expression (12) for the capacitor c_c is used as an initial guess for the HB−AG optimization with 20 harmonic terms. The final capacitor value is $c_{cm} = 10$ pF.
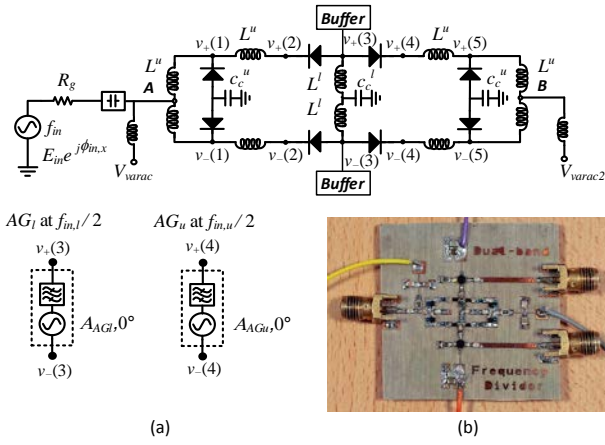
Fig. 17 Dual−band frequency divider. (a) Schematic. (b) Photograph of the prototype built in Rogers 4003C substrate $(\varepsilon_r = 3.38, H = 0.508 \text{ mm})$. Output signals are extracted with a source−follower buffer based on the transistor NE3210S01.

Fig. 18 presents the result of the individual analyses of the parallel−varactor divider (neglecting the series−varactor cell) and the series−varactor divider (neglecting the two parallel varactor cells). This result can be compared with the one obtained when performing a HB−AG simulation of the full divider in Fig. 17, taking into account the coupling between the two types of cells. The number of harmonic terms is $NH = 20$ in the three cases. To analyze the lower frequency band of the dual divider, the AG (AG_l) is connected in differential manner between the nodes $v_+(3)$ and $v_-(3)$, corresponding to the series−varactor cell. To analyze the upper frequency band, the AG (AG_u) is connected in differential manner between the nodes $v_+(4)$ and $v_-(4)$, of the parallel−varactor sub−circuit [Fig. 17(a)]. The coupling tends to separate the bands but gives rise to a reduction of the division thresholds, attributed to the presence of a higher number of varactor diodes in the two cases.
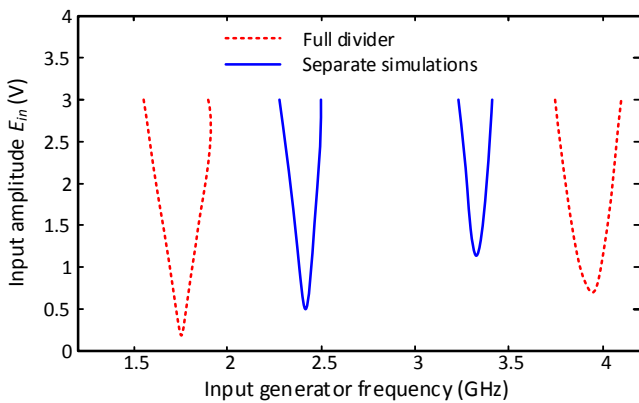

Fig. 18 Input−sensitivity curves of the two dividers based on a series−varactor cell and two parallel−varactor cells optimized in HB in a separate manner, with $NH = 20$ harmonic components. The results are compared with those obtained when simulating the full divider configuration in Fig. 17 with $NH = 20$ harmonic components.

As shown in Fig. 18, under coupled conditions the two

division bands are centered about $f_{in} = 1.72$ GHz and $f_{in} = 3.97$ GHz, respectively. Then the additional capacitors c_c^l and c_c^u of the two types of cells can be separately calculated to maximize the division bandwidth about each frequency. The resulting values are $c_c^l = 10$ pF for the lower division band and $c_c^u = 0.43$ pF for the upper division band. The corresponding input−sensitivity curves are shown in Fig. 19(a) and Fig. 19(b), where they can be compared with the ones obtained with a common c_c, having an intermediate magnitude: $c_c = 4.4$ pF. Measurements have been superimposed for both the original and optimized values. The output signal is extracted with a source−follower buffer based on the transistor NE3210S01.
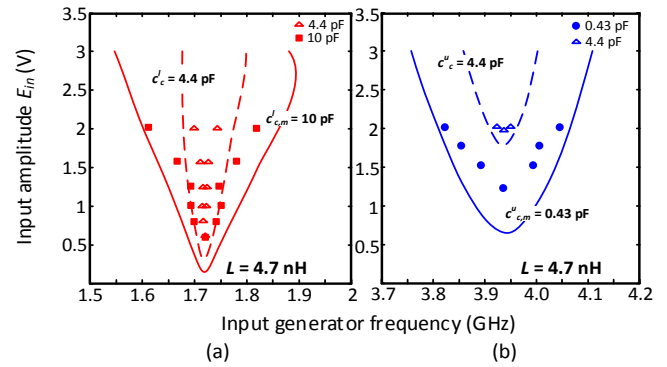

Fig. 19 Influence of capacitor c_c on the division bandwidth for fixed $L = 4.7$ nH. (a) Sensitivity curves at the lower frequency band for intermediate and optimized values of c_c. (b) Sensitivity curves at the upper frequency band. Measurements are superimposed.

The solution curves in terms of the subharmonic amplitude have been calculated for the element values $L = 4.7$ nH and $c_{c,m}^l = 10$ pF in the series−varactor cell, and $L = 4.7$ nH and $c_{c,m}^u = 0.43$ pF, in the parallel−varactor cells. Results are shown in Fig. 20, where they can be compared with the measurement points. At $E_{in} = 2$ V, the two division bandwidths are $BW_L = 259$ MHz and $BW_U = 251$ MHz at the low and high frequency band respectively. Fig. 21(a) and Fig. 21(b) show the measured divided−solution waveforms obtained with the dual−band divider at $f_{in} = 1.78$ GHz and at $f_{in} = 3.92$ GHz, respectively, both exhibiting a pronounced frequency division.
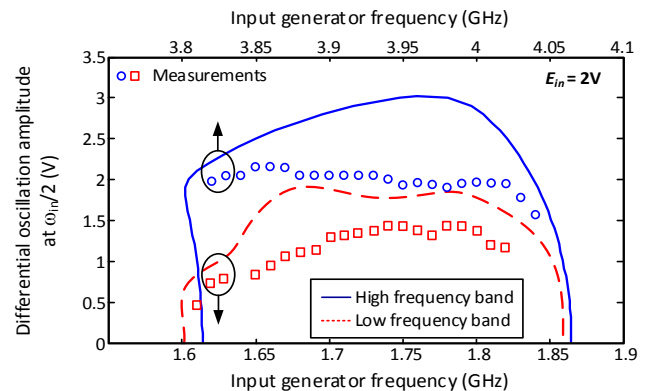
Fig. 20 Variation of the subharmonic amplitude versus the input frequency in each of the two division bands, obtained for constant $E_{in} = 2\,\text{V}$. Measurements have been superimposed.
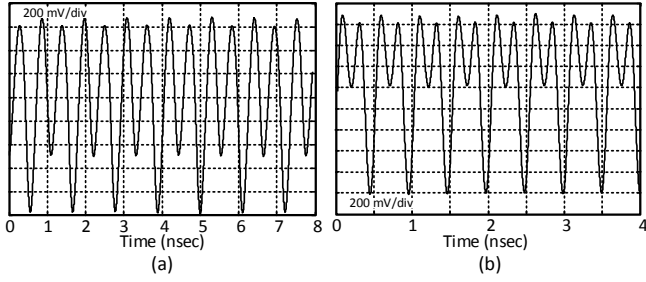

Fig. 21 Measured divided−solution waveforms obtained with the dual−band divider. (a) $f_{in} = 1.78\,\text{GHz}$. (b) $f_{in} = 3.92\,\text{GHz}$.

Finally, the phase−noise spectrum at each of the two coexistent frequency−division bands, with respective input frequencies $f_{in} = 1.78\,\text{GHz}$ and $f_{in} = 3.92\,\text{GHz}$, has been calculated and compared with the spectrum of the input source at each of the two frequencies. The results are shown in Fig. 22. The measured spectra are superimposed with good agreement. The respective corner frequencies Ω_0 are different, which can be attributed to differences in the three main magnitudes affecting the corner: $\left|Y_\phi\right|$, V_1 and $\alpha_\phi - \alpha_V$.
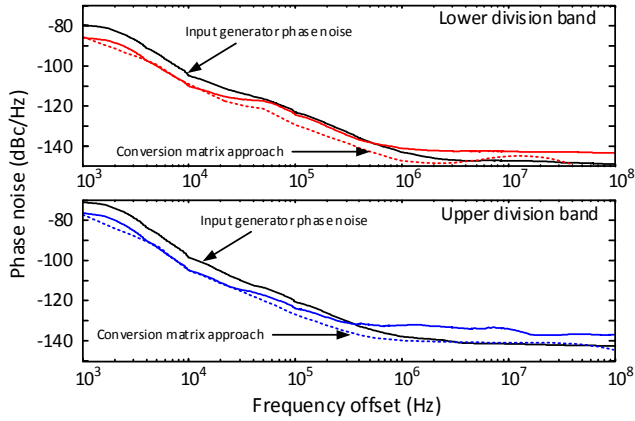

Fig. 22 Phase−noise spectrum at the central frequencies of the two coexistent division bands. Each spectrum is compared with that of the input source. Measurements are superimposed in the two cases. (a) $f_{in} = 1.78\,\text{GHz}$, in the lower division band. (b) $f_{in} = 3.92\,\text{GHz}$, in the higher division band.

C. Pre−setting of the two division bands

The possibility to center the two division bands at specified frequency f_{inl} and f_{inu} has been investigated. Due to the coupling effect, one cannot center one band without affecting the other. This is shown in the analysis of Fig. 23, with measurement superimposed. Variations in L_l (L_u) enable a large shift of the lower (upper) division band, with a smaller undesired shift in the upper (lower) band. To circumvent this problem, an optimization procedure has been developed, based on the simultaneous optimization of two identical copies of the circuit, with identical element values L_l, c_l, L_u and c_u (Fig. 24). The first circuit copy operates at the desired central frequency of the lower division band, f_{inl}, and is analyzed with an AG (AG_l) at

$f_{AGl} = f_{inl}/2$, with an input−source phase $\phi_{in,l}$. This AG is connected between the nodes of the series−varactor cell [Fig. 24(a)]. The second circuit copy operates at the desired central frequency of the upper division band, f_{inu}, and is analyzed with an AG (AG_u) at $f_{AGu} = f_{inu}/2$, with an input−source phase $\phi_{in,u}$. This AG is connected at one of the two parallel−varactor cells [Fig. 24(b)].
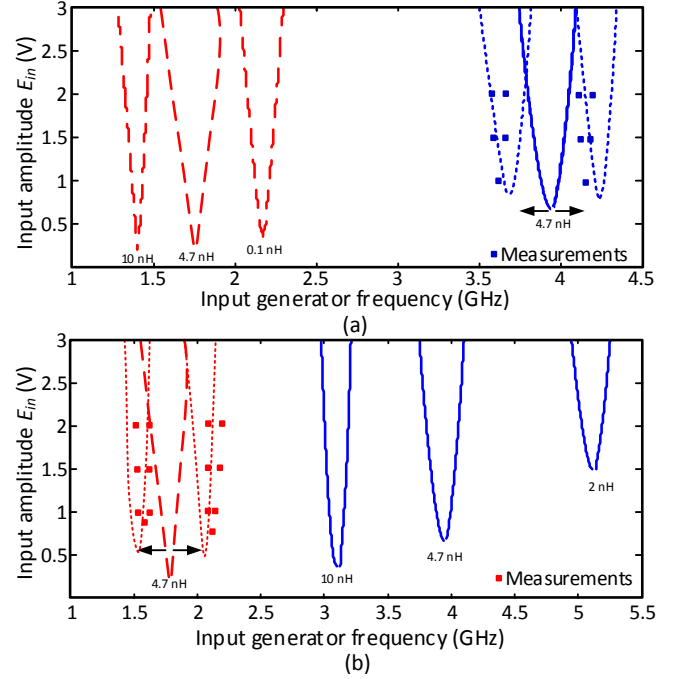

Fig. 23 Global operation of the dual−band frequency divider, analyzed in the plane defined by ω_{in} and E_{in}. (a) Effect of the variation of the L^l to tune the lower frequency band. (b) Effect of the variation of L^u to tune the upper frequency band.

The two copies of the circuit are simultaneously analyzed with two−tone HB, at the two fundamental frequencies $f_{AGl} = f_{inl}/2$ and $f_{AGu} = f_{inu}/2$, with 0 intermodulation order, since each circuit operates at a different frequency. Because the intermodulation order is 0, the analysis frequencies are the $NH=20$ harmonics of f_{AGl} and the $NH=20$ harmonics of f_{AGu}, so the computational cost is bearable. Because the aim is to preset the division threshold, the amplitude of the two AGs is set to very small value ε. Then the two circuits (with common design values) are simultaneously optimized to fulfil:

$$Y_{AGl} = \left(L_l, c_l, L_u, c_u, \phi_{in,l}, \phi_{in,u}\right) = 0$$
$$Y_{AGu} = \left(L_l, c_l, L_u, c_u, \phi_{in,l}, \phi_{in,u}\right) = 0 \tag{38}$$

with the pure two tone HB system as an inner tier. The initial values of the elements L_l, c_l, L_u and c_u are those resulting from the separate optimizations of the series−varactor cell (L_l^o, c_l^o) and the parallel−varactor cell (L_u^o, c_u^o). On the other hand, the input sensitivity will be slightly different in each division band, so the input source should have different amplitude in each of the two copies of

the circuit. The first (second) copy, operating at f_{inl} (f_{inu}) will have input amplitude E_{inl} (E_{inu}). The initial values of E_{inl} and E_{inu} will correspond to those resulting from the initial separate optimization of the series−varactor divider and parallel−varactor divider, given by $E_{inl}^{\,o}$ and $E_{inu}^{\,o}$, respectively.

The complex system (38) is over−dimensioned, as it composed by two complex equations in six optimization variables, which should facilitate the convergence. The system forces the divider to operate at the two specified frequencies f_{inl} and f_{inu}. To actually center the two division curves about these values, one should reduce the division threshold E_{inl} and E_{inu} as much as possible. This can be done by sweeping down the higher of the two magnitudes from the one obtained with the separate optimization (either $E_{inl}^{\,o}$ or $E_{inu}^{\,o}$). System (38) is optimized at each sweep step. The different stages of the design procedure are indicated in the flowchart of Fig. 25. As an example, this procedure has been applied to center the two division bands at $f_{inl} = 2\ \text{GHz}$ and $f_{inu} = 3.5\ \text{GHz}$. Fig. 26(a) shows the variation of the optimization elements that exhibit the largest variation when decreasing E_{inl}. The actual centering of the two division bands about f_{inl} and f_{inu} is demonstrated with an independent simulation of the divider, when operating at each of the two division bands [Fig. 26(b)]. As can be seen, with the simultaneous optimization it has been possibly to accurately center the "merged" dual−band divider at the specified frequencies f_{inl} and f_{inu}.

1. Optimize the values of the (isolated) series-varactor cell at f_{inl}
- Introduce one AG in the HB simulation
- Set AG frequency to $f_{AG} = f_{inl}/2$
- Select optimum L solving $Y_{AG}(E_{in}, \phi_{in}, L) = 0$
- Select optimum c_c solving $Y_{AG}(E_{in}, \phi_{in}, c_c) = 0$
- Final values L_l^o and c_l^o

2. Optimize the values of the (isolated) parallel-varactor divider (with 2 cells) at f_{inu}
- Set AG frequency to $f_{AG} = f_{inu}/2$
- Select optimum L solving $Y_{AG}(E_{in}, \phi_{in}, L) = 0$
- Select optimum c_c solving $Y_{AG}(E_{in}, \phi_{in}, c_c) = 0$
- Final values L_u^o and c_u^o

3. Optimization of two circuit copies of the complete dual-band divider
- Copy 1 (Copy 2) operates at $f_{inl}/2$ ($f_{inu}/2$) with E_{inl}, $\phi_{in,l}$ (E_{inu}, $\phi_{in,u}$).
- Introduce one AG at $f_{inl}/2$ in Copy 1
- Introduce one AG at $f_{inu}/2$ in Copy 2 at one of the parallel-varactor cells
- Use two-tone HB (0 intermodulation order) to optimize the copies (35)
- Initial values for the optimization (L_l^o, c_l^o, L_u^o, c_u^o, E_{inl}^o, E_{inu}^o)
- Final values: (L_l, c_l, L_u, c_u, E_{inl}, E_{inu})

4. Evaluate the input-sensitivity curve
- Keep element values at: L_l, c_l, L_u, c_u
- Analyze the final circuit in each of the two frequency bands
- Sweep ω_{in} solving $Y_{AG}(E_{in}, \phi_{in}, \omega_{in}) = 0$ at each step
- Trace E_{in} versus ω_{in}

Fig. 25 Flowchart indicating the steps to be taken for the optimized design of the dual−band frequency divider.
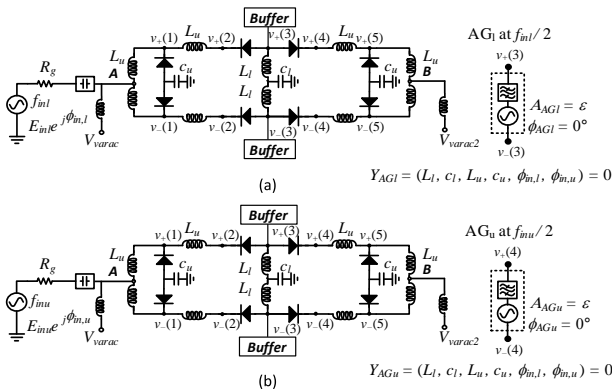

Fig. 24 Duplicated circuit for the optimization procedure. (a) Copy of the circuit operating at the central frequency of the lower division band f_{inl}. (b) Copy of the circuit operating at the central frequency of the upper division band f_{inu}. The two copies are simultaneously optimized with two AGs at $f_{AGl} = f_{inl}/2$ and $f_{AGu} = f_{inu}/2$, in order to fulfill (38).
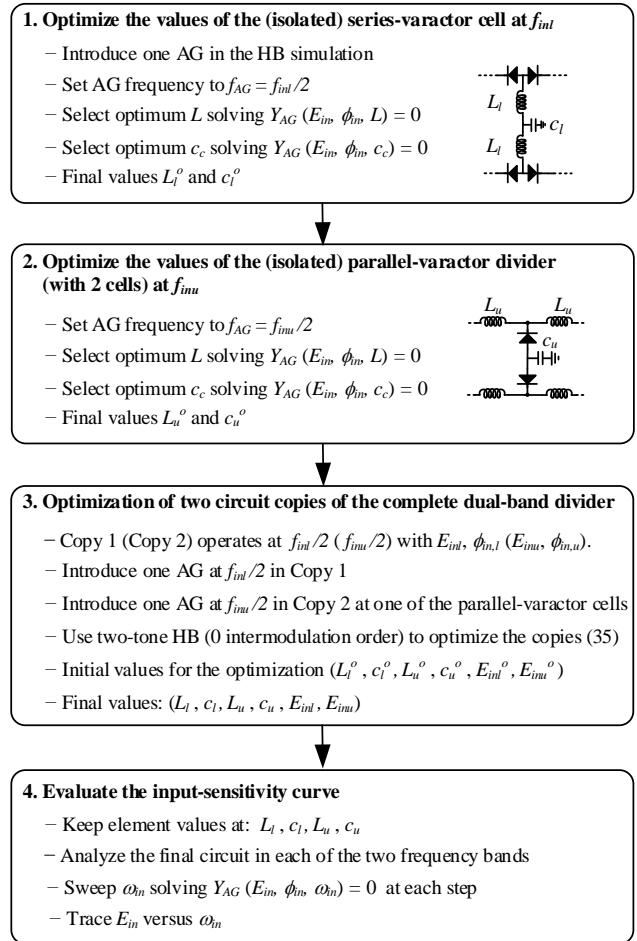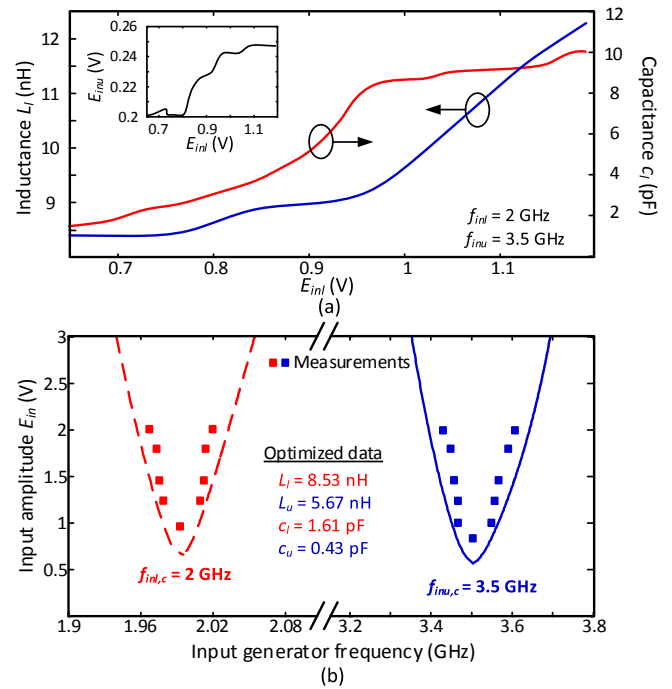

Fig. 26 Use of conditions (38) to center the two division bands at the specified frequencies $f_{inl} = 2\ \text{GHz}$ and $f_{inu} = 3.5\ \text{GHz}$. (a) Variation of two of the optimization variables, L_l, c_l, when decreasing E_{inl}. (b) Validation with an independent analysis of the two division bands.

V. Conclusion

A design methodology for a recently proposed frequency−divider configuration based on varactor−inductor cell has been proposed. The method derives from an initial analytical study of a single−cell divider, which provides insight into the impact of the various circuit elements on the input−amplitude threshold and the frequency bandwidth. The inductors of the divider topology enable the shift of the frequency−division band and an additional capacitor enables the reduction of the input−amplitude threshold. With a higher number of cells, the two element types still enable these two separate actions, as has been verified with a full harmonic balance analysis, using an auxiliary generator at the divided frequency. Two different applications have been demonstrated: a dual−phase divider, based on the use of a Marchand balun, and a dual−band frequency divider, based on a novel configuration in which a series−varactor cell is embedded between two parallel−varactor cells. A simple synthesis method is presented to center the two division bands at the desired values. The techniques have been applied to three prototypes at 2.15 GHz, 1.85 GHz and 1.75 GHz / 3.95 GHz, respectively.

References

[1] W. Lee and E. Afshari, "Low−Noise Parametric Resonant Amplifier," *IEEE Trans. Circuits and Systems I*, vol.58, no.3, pp.479−492, Mar., 2011.

[2] W. Lee and E. Afshari, "Distributed Parametric Resonator: A Passive CMOS Frequency Divider," *IEEE J. Solid−State Circuits*, vol.45, no.9, pp.1834−1844, Sept., 2010.

[3] H. R. Rategh and T. H. Lee, "Superharmonic injection−locked frequency dividers," *IEEE J. Solid−State Circuits*, vol. 34, no. 6, pp. 813−821, Jun. 1999.

[4] R. Quere, E. Ngoya, M. Camiade, A. Suérez, M. Hessane, and J. Obregón, "Large signal design of broadband monolithic microwave frequency dividers and phase−locked oscillators," *IEEE Trans. Microwave Theory Techn.,* vol. 41, pp. 1928–1938, Nov. 1993.

[5] A. Suárez, J.C. Sarkissian, R. Sommet, E. Ngoya, and R. Quere, "Stability analysis of analog frequency dividers in the quasi−periodic regime," *IEEE Microw. Guided Wave Lett.*, vol.4, no.5, pp.138−140, May 1994.

[6] A. Suárez, R. Quéré, *Stability Analysis of Nonlinear Microwave Circuits*. Boston, MA: Artech House, 2003.

[7] A. Suárez, *Analysis and Design of Autonomous Microwave Circuits*. Hoboken, NJ: Wiley IEEE Pres, 2009.

[8] F. Ramírez, M. Pontón, S. Sancho, A. Suárez, "Phase−Noise Analysis of Injection−Locked Oscillators and Analog Frequency Dividers", *IEEE Trans. Microw. Theory Techn.,* vol. 56, no.2, pp. 393−407, 2008.

[9] S. Qin, Q. Xu and Y. E. Wang, "Nonreciprocal Components With Distributedly Modulated Capacitors," *IEEE Trans. Microw. Theory Techn.,* vol. 62, no. 10, pp. 2260– 2272, Oct.2014.

[10] M. Pontón and A. Suárez, "Analysis of a frequency divider by two based on a differential nonlinear transmission line," *IEEE MTT−S Int. Microw. Symp. Dig.*, Phoenix, AZ, USA, 2015, pp.1−3.

[11] S.A. Kian and I.D. Robertson, "Analysis and design of impedance−transforming planar Marchand baluns," *IEEE Trans. Microw. Theory Techn.*, vol.49, no.2, pp.402−406, Feb., 2001.

[12] L. Zhang and H. Wu, "A double−balanced injection−locked frequency divider for tunable dual−phase signal generation," *IEEE Radio Frequency Integrated Circuits (RFIC) Symposium*, San Francisco, CA., 2006.

[13] V. Arana, A. Suarez, P. Dorta, "Dual−band frequency divider based on oscillation control," *IEEE MTT−S Int. Microw. Symp. Dig.*, Fort Worth, TX, USA, Jun. 2004, vol.3, pp.1501−1504.

[14] J. Guckenhehimer and P. Holmes, *Nonlinear Oscillations, Dynamical Systems, and Bifurcations of Vector Fields*, Springer Verlag, NY, 1983.

[15] [Online].Available:http://www.skyworksinc.com/uploads/docum ents/SMV123x_Series_200058V.pdf

[16] F. Ramírez, E. de Cos, and A. Suárez, "Nonlinear analysis Tools for the Optimized Design of Harmonic−Injection Dividers," *IEEE Trans. on Microwave Theory and Techn.*, vol. 51, no. 6, pp. 1752–1762, Jun., 2003.

[17] K. Kurokawa, "Noise in synchronized oscillators," *IEEE Trans. Microw. Theory Techn.*, vol. 16, no. 4, pp. 234–240, Apr., 1968.

[18] J.M. Paillot, J.C. Nallatamby, M. Hessane, R. Quere, M. Prigent and J. Rousset, "A general program for steady state, stability, and FM noise analysis of microwave oscillators," *IEEE MTT−S Int. Microwave Symp. Dig.*, Dallas, TX, USA, 1990, pp. 1287–1290.

[19] V. Rizzoli, F. Mastri, and D. Masotti, "General noise analysis of nonlinear microwave circuits by the piecewise harmonic−balance technique," *IEEE Trans. Microw. Theory Techn.,* vol. 42, no. 5, pp. 807–819, May 1994.

[20] Y. Park, S. Chakraborty, C.−H. Lee, S. Nuttinck, J. Laskar, "Wide−band CMOS VCO and frequency divider design for quadrature signal generation," *IEEE MTT−S Int. Microw. Symp. Dig.*, Fort Worth, TX, USA, Jun. 2004, vol.3, pp.1493−1496.

[21] J. Jugo, J. Portilla, A. Anakabe, A. Suárez and J.M. Collantes, "Closed–loop stability analysis of microwave amplifiers," *IEEE Electron. Lett.*, vol. 37, no. 4, pp. 226−228, 2001.

Mabel Pontón (S'08–M'11) was born in Santander, Spain. She received the Telecommunication Engineering degree from the University of Cantabria, Spain in 2004, Masters in Information Technologies and Wireless Communications Systems and Ph.D. degree from the University of Cantabria, Santander, Spain, in 2008 and 2010, respectively. In 2006, she joined the Communications Engineering Department of University of Cantabria.

From 2011 to 2013 she was with the Group of Electronic Design and Applications (EDA) at Georgia Institute of Technology, Atlanta, GA as a Post−Doctoral Research Fellow. Her research interests are focused on the nonlinear analysis and simulation of radiofrequency and microwave circuits, with emphasis on phase−noise, stability and bifurcation analysis of complex oscillator topologies.

Almudena Suárez (M'96–SM'01–F'12) was born in Santander, Spain. She received the Electronic Physics and Ph.D. degrees from the University of Cantabria, Santander, Spain, in 1987 and 1992, respectively, and the Ph.D. degree in electronics from the University of Limoges, Limoges, France, in 1993.

She is currently a Full Professor with the Communications Engineering Department, University of Cantabria. She co−authored *Stability Analysis of Nonlinear Microwave Circuits* (Artech House, 2003) and authored *Analysis and Design of Autonomous Microwave Circuits* (IEEE−Wiley, 2009).

Prof. Suárez is a member of the Technical Committees of the IEEE Microwave Theory and Techniques Society (IEEE MTT−S) International Microwave Symposium (IMS) and the European Microwave Conference. She was an IEEE Distinguished Microwave Lecturer from 2006 to 2008. She is a member of the Board of Directors of the *European Microwave Association*. She is the Editor−in−Chief of the International Journal of Microwave and Wireless Technologies (Cambridge University Press). She was the co−chair of IEEE Topical Conference on RF Power Amplifiers (PAWR) in 2014 and 2015.